Journal of
Synchrotron Radiation

ISSN 0909-0495

Received 18 February 2009
Accepted 13 October 2009

First experiments on the Australian Synchrotron Imaging and Medical beamline, including investigations of the effective source size in respect of X-ray imaging

Andrew W. Stevenson,[a]* Sheridan C. Mayo,[a] Daniel Häusermann,[a,b,c] Anton Maksimenko,[b] Richard F. Garrett,[b,d] Christopher J. Hall,[c,e] Stephen W. Wilkins,[a,e] Robert A. Lewis[c,e] and Damian E. Myers[a,f]

[a]CSIRO Materials Science and Engineering, Private Bag 33, Clayton South, Victoria 3169, Australia, [b]Australian Synchrotron, 800 Blackburn Road, Clayton, Victoria 3168, Australia, [c]Monash Centre for Synchrotron Science, Monash University, Melbourne, Victoria 3800, Australia, [d]Bragg Institute, ANSTO, PMB 1, Menai, NSW 2234, Australia, [e]School of Physics, Monash University, Melbourne, Victoria 3800, Australia, and [f]Department of Medicine (RMH/WH), University of Melbourne, Parkville, Victoria 3050, Australia. E-mail: andrew.stevenson@csiro.au

The Imaging and Medical beamline at the Australian Synchrotron achieved 'first light' in December 2008. Here, the first experiments performed on the beamline are reported, which involved both X-ray imaging and tomography studies for a range of samples. The use of a plastic-edge phantom for quantitative measurements of contrast and resolution proved to be very instructive and helped to confirm certain parameter values such as the effective horizontal source size, detector resolution and average X-ray energy for the polychromatic beam.

Keywords: X-ray imaging; X-ray tomography; phase contrast; source size.

1. Introduction

The Imaging and Medical beamline (IMBL) at the Australian Synchrotron [3.0 GeV ($1/\gamma$ = 170 µrad); 200 mA; circumference 216 m; see Boldeman & Einfeld (2004) for a description of the physics design] achieved 'first light' in December 2008. This paper reports the first experiments by a team from CSIRO, Monash University and the Australian Synchrotron. These experiments involved both X-ray imaging and tomography studies for various samples, including medical/biomedical and materials-science applications. The focus of this paper is on the imaging results obtained, including some fundamental experiments aimed at estimating the effective X-ray source size.

The experiments were performed in the second hutch (1B), with a minimum source-to-sample distance (R_1) of 20 m. Sample-to-detector distances (R_2) of up to 3 m were used. The current insertion device is an Advanced Photon Source (APS) type-A permanent-magnet wiggler, which was operated with a gap of 55 mm to protect a temporary Be window from excessive thermal loading. Given that hutch 2B (31.7–40.0 m) and the satellite building (including hutches 3A and 3B; sample position at 136 m) have already been constructed, there is interest in the quality of the X-ray imaging that can be achieved with this interim insertion device, and, ultimately, with the future superconducting multipole wiggler. The RMS electron beam size in the straight sections at the Australian Synchrotron is 320 µm horizontally and 16 µm vertically (1% coupling), with distributed dispersion of 0.1 m. These values correspond to Gaussian FWHM of 754 µm and 38 µm, respectively. The electron-beam deviation caused by the field of the APS wiggler is small in comparison with the electron-beam size and so it is the latter which dictates the X-ray source size. This large horizontal source size and the 20:1 aspect ratio are important factors to be investigated in respect of X-ray imaging on this beamline, especially with reference to spatial coherence for propagation-based phase-contrast imaging. In the case of analyzer-based phase-contrast imaging, similar issues will arise if the plane of diffraction is vertical.

The experiment end-station in the satellite building will not only enable the use of a wide X-ray beam for imaging large objects but also significantly increase the demagnification of the source. Reduced source demagnification will significantly limit the degree of phase contrast achievable in the horizontal direction in hutch 1B.

In conventional treatment of X-ray imaging, and implicit in the above discussion, the X-ray source is regarded as totally incoherent within the range of the source size. In reality, and especially in the case of synchrotron radiation, some degree of coherence across the spatial extent of the source is possible. Such partial coherence of the source may affect image quality, and our aim is to measure the effective source size.

2. Experimental

The synchrotron operated at 200 mA, with a beam decay to about 150 mA in the 12 h between injections. The experiments were performed in hutch 1B, with the beam delivered from the Be window in upstream hutch 1A through a He-filled tube. The He reduced ozone production and protected the 0.5 mm Be window in the aggressive environment caused by the white beam (no monochromators having been installed as yet). The high X-ray flux also necessitated the use of polished Al filters (total thickness 6.0 mm) to protect the CCD detector and minimize damage to the more sensitive samples. The filters were selected so that the X-ray image quality, after processing, was not noticeably compromised. Fig. 1 shows a schematic diagram of the experimental configuration used.

The CCD used was a 10 MHz 16M FDI-VHR camera, capable of 12-bit and 16-bit operation, supplied by Photonic Science. It was operated at approximately 241 K *via* the multi-stage Peltier cooling, and with a chilled water supply to remove the heat generated by the Peltier. The CCD has 4872 × 3248 (horizontal × vertical) 7.4 µm pixels, is optically bonded to a straight fibre-optic bundle (no magnification), and employs a (P43) Tb-doped Gadox (gadolinium oxysulphide) input phosphor (5 mg cm^{-2}). It is optimized for X-rays in the 2–30 keV range. The images were pre-processed in conjunction with flat-field and dark-current images, *i.e.* images without an object and without X-rays, respectively. Correlation of sequences of image frames from a static sample, collected over a period of time, showed no significant drift present, *i.e.* high correlation coefficients and (translational) movement of less than a single pixel.

The APS wiggler has 28 × 8.5 cm periods with a total length of 2.4 m. At a gap of 55 mm, the field is approximately 0.24 T and the deflection parameter K is 1.9 (see Lai *et al.*, 1993; http://aps.anl.gov/Science/Publications/techbulletins/TB-11.pdf). This quite small K-value means that this insertion device is behaving with considerable undulator character (see Clarke, 2004, p. 43). The critical energy is 1.4 keV and the first-order harmonic energy is 0.36 keV. The program *SPECTRA 8.0* (Tanaka & Kitamura, 2001; http://radiant.harima.riken.go.jp/spectra/index_e.html) was used to calculate the spectral brightness (Mills *et al.*, 2005) as a function of energy in steps of 0.1 keV, using the storage-ring parameter values from http://radiant.harima.riken.go.jp/spectra/asp.prm. This spectrum was converted into flux density within 1 mm^2 at the centre of the beam and 20 m from the source. Allowance was then made for the effect of the various filters, windows and materials present in the beam path, and for the quantum efficiency of the detector. The spectrum calculation was performed for both a wiggler and an undulator; the final results shown in Fig. 2 have been smoothed by using a 'running average' over 11 data points. The undulator calculation yields, as expected, a (final) spectrum peak with considerable harmonic structure. Table 1 shows the parameter values which characterize the (wiggler) spectrum at each stage after inclusion of the various factors (without applying the running average). The final results for the corresponding undulator calculation are also given in Table 1.

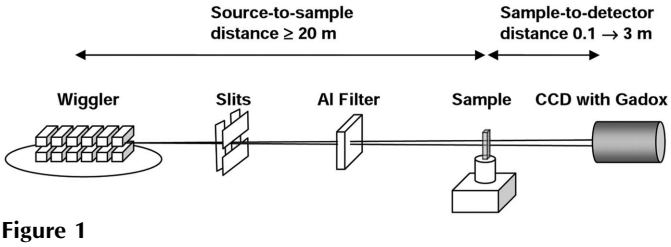

Figure 1
Schematic diagram of the experimental layout used for these experiments at IMBL.

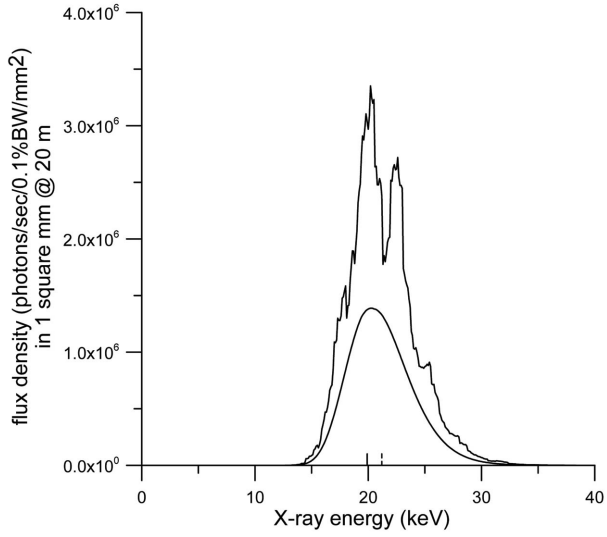

Figure 2
Calculated spectrum used for X-ray imaging and tomography experiments. The short solid line indicates the peak position (19.9 keV), the short dashed line the weighted-average energy (21.2 keV), for the smooth curve (wiggler-based calculation). The jagged curve is for the undulator-based calculation.

3. Results

Fig. 3 shows X-ray images collected for (*a*) a gum leaf (R_1 = 20.8 m; R_2 = 155 cm) and (*b*) a coarse-fibre paper sample (R_1 = 20.3 m; R_2 = 159 cm). The experimental magnification $M = (R_1 + R_2)/R_1$ is approximately 1.08. There is little X-ray absorption for these samples and the dominant contrast mechanism is phase contrast. The 'salt and pepper' noise near the edges of these images is due to the rapid drop in beam flux here, an effect exacerbated by the flat-field correction.

In Fig. 4 the images of three fixed mouse tibiae are shown, one in each column [see Cornish *et al.* (2002) for details of the samples]. The images reveal that the tibiae have quite distinct trabecular microstructures. The first row corresponds to M = 1.00; the second row to M = 1.08; the third row to M = 1.15. Absorption- and phase-contrast effects are present in these images to varying degrees, with the M = 1.00 (essentially 'contact') images being dominated by absorption contrast. Whilst the effects are quite subtle, the increase in phase contrast and reduced demagnification of the X-ray source as R_2 increases from 158 cm to 305 cm can be detected.

Table 1
Values of parameters used to characterize the X-ray spectrum after inclusion of the effects of windows, filters and other materials present in the beam path (wiggler-based calculation).

The final row (in italics) corresponds to an undulator-based calculation of the spectrum. The Al filter thickness subsumes a 12 μm Al window in the CCD for excluding light. We also note that the number of visible photons produced in the CCD is a function not only of the number of X-ray photons but also of their energy. Allowance for this energy dependence has little effect in the current context however, *e.g.* the final value of the weighted-average energy changes to 21.6 keV. NA = not applicable.

Factor†	Maximum flux density [photons s^{-1} (0.1% bandwidth)$^{-1}$ mm^{-2}]	Energy (keV) for maximum flux density	FWHM (keV)	Weighted-average energy (keV)
None	3.4×10^{13}	1.9	NA	NA
+ He (6.5 m)	2.3×10^{13}	2.9	3.6	4.3
+ Be (0.5 mm)	9.4×10^{12}	4.5	3.8	5.8
+ Sigradur (0.1 mm)‡	6.8×10^{12}	5.0	3.9	6.2
+ Kapton (0.1 mm)	5.0×10^{12}	5.5	4.0	6.7
+ graphite (1 mm)	9.3×10^{11}	7.8	4.5	8.9
+ Al (6.0 mm)	9.1×10^{6}	21.3	6.7	22.2
+ Gd_2O_2S:Tb (5 mg cm^{-2})§	1.4×10^{6}	19.9	6.2	21.2
+ Gd_2O_2S:Tb (5 mg cm^{-2})§	*8.3×10^{6}*	*22.5*	*4.0*	*21.3*

† All absorption coefficients are calculated using total cross sections (Zschornack, 2007). ‡ Glassy carbon CCD window. § CCD quantum efficiency calculated as $1 - \exp(-\mu_m \rho_s)$, where μ_m is the energy-dependent mass absorption coefficient and ρ_s is the 'surface density' (or 'phosphor concentration'); a more rigorous calculation of the energy-dependent CCD response, to be reported elsewhere, does not have any significant effect in the current context

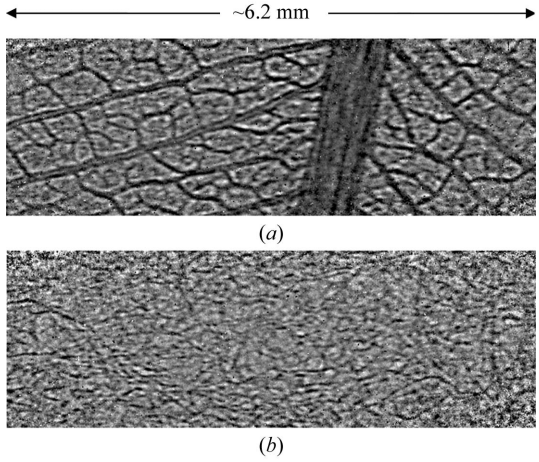

Figure 3
X-ray phase-contrast images obtained for (*a*) a gum leaf and (*b*) a coarse-fibre paper sample.

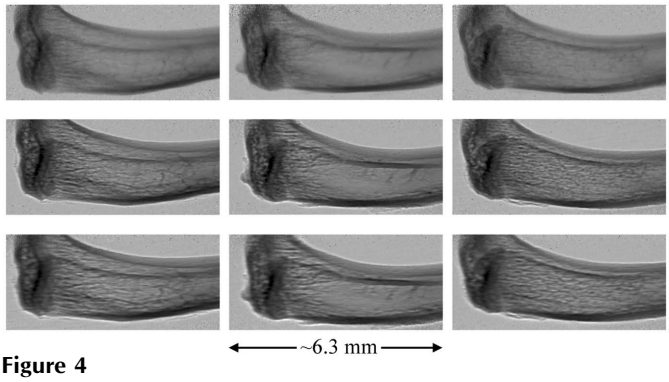

Figure 4
X-ray images obtained for three fixed mouse tibiae. The tibiae were obtained from mice treated with control (left column), α-MSH (middle column) and leptin (right column). Details are provided by Cornish *et al.* (2002). The rows correspond to, from top to bottom, $R_1 = 22.5$ m and $R_2 = 8$ cm ($M = 1.00$); $R_1 = 20.5$ m and $R_2 = 158$ cm ($M = 1.08$); $R_1 = 20.5$ m and $R_2 = 305$ cm ($M = 1.15$).

The image of the dragon-fly presented in Fig. 5 is the result of combining more than 80 individual images, obtained by scanning the sample in 2 mm steps vertically and 6 mm steps horizontally across the beam to create a montage ($R_1 = 20.8$ m; $R_2 = 155$ cm). The images to the right are magnified sections from a wing and the head. Whilst absorption contrast is present, phase contrast is again the dominant mechanism, especially for the delicate wing structure [see Snigirev *et al.* (1995) and Wilkins *et al.* (1996) for the fundamentals of propagation-based X-ray phase-contrast imaging].

A tomography data set was collected for another mouse tibia. A total of 900 images were collected over a 180° rotation in 0.2° steps with $R_1 = 21.6$ m and $R_2 = 23$ cm ($M = 1.01$). In addition to the usual pre-processing steps mentioned earlier, a phase-retrieval step was included for the tomography data. The algorithm used was that of Paganin *et al.* (2002), which assumes a homogeneous object and is based on the transport-of-intensity equation (Teague, 1983). It requires a value of δ/β ($= -2\varphi/\mu$) for the object, where the X-ray refractive index is given by $n = 1 - \delta - i\beta$, φ is the phase shift per unit length, and

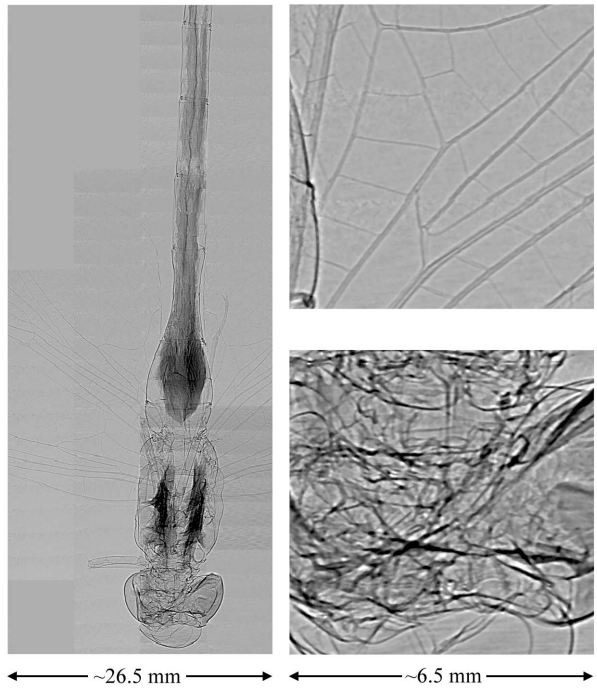

Figure 5
X-ray image of a dragon-fly obtained by combining more than 80 individual images to create a montage. Magnified sections from a wing and the head are shown on the right.

μ is the linear absorption coefficient (all these quantities being energy- or wavelength-dependent). As the results are not particularly sensitive to this parameter, we used a spectrally weighted average value (180) for hydroxylapatite [$Ca_5(PO_4)_3OH$; $\rho = 3.18$ g cm^{-3}], the major component of osseous tissue. A cone-beam reconstruction was performed using the conventional *FDK* algorithm (Feldkamp *et al.*, 1984). These data processing and analysis operations were all performed using the *X-TRACT* (version 4) software package; http://ts-imaging.net/Services/. Figs. 6(*a*)–6(*d*) show reconstructed (*xy*) slices perpendicular to the direction of the tibia shaft at 1.72, 1.36, 0.99 and 0.62 mm from the top of the tibia. Fig. 6(*e*) is a reconstructed *yz* slice and Fig. 6(*f*) is a reconstructed *xz* slice, both at the longitudinal mid-line of the tibia.

The images presented thus far are all remarkable in that the relatively large horizontal source size and 20:1 aspect ratio do not appear to be significant factors for the geometrical conditions being employed. Close examination of the images, especially those for the tibiae in Fig. 4, do indicate that the resolution of fine details is superior in the vertical direction than in the horizontal. However, the degree of improvement is not consistent with a simplistic view of the effect of the X-ray source. Given that these observations are qualitative and to a certain extent subjective, it was decided that images should be collected for a plastic-edge phantom.

The plastic-edge phantom was studied previously with a laboratory-based microfocus X-ray source (Gureyev *et al.*, 2008). It provides a means of obtaining quantitative contrast and resolution values, and of simultaneously checking vertical and horizontal directions. This simple phantom consists of two 100 µm-thick polyethylene sheets, partially overlapped to have edges running vertical and horizontal. Given our experimental conditions, in particular the X-ray energy range, this phantom provides images with both absorption and phase contrast, but dominated by the latter, in the form of characteristic single black–white fringes. The images were analysed to provide contrast and resolution values. The observed (experimental) contrast values are obtained from the difference between the maximum and minimum intensity values divided by their sum. The observed resolution values are obtained from the spatial separation of these features, referred to the object plane. The observed data values for vertical and horizontal edges, affected by the horizontal and vertical source dimensions, respectively, are listed in Table 2 as a function of R_2 ($R_1 = 21.6$ m). The estimated standard deviations (e.s.d.s) for the contrast values are 0.3% and for the resolution values are 2 µm (these values are smaller than the effective pixel size as the positions of the maximum and minimum intensities were extracted from the data by fitting). These e.s.d.s are consistent with the agreement between values of contrast and resolution obtained for a single polyethylene edge and for a single polyethylene edge overlapped by a single polyethylene sheet.

Table 2
Summary of experimental and theoretical (least-squares fitting) contrast and resolution values for a plastic-edge phantom.

Errors associated with the experimental quantities are discussed in the text.

R_2 (cm) [M]	Plastic-edge disposition	Contrast C (%) experiment	Contrast C (%) calculated	Resolution R (µm) experiment	Resolution R (µm) calculated
19.8 [1.01]	Vertical	1.2	0.82	40	39
19.8 [1.01]	Horizontal	1.3	0.84	41	39
69.8 [1.03]	Vertical	2.6	2.2	43	44
69.8 [1.03]	Horizontal	3.5	3.0	36	38
119.8 [1.06]	Vertical	3.0	2.6	55	54
119.8 [1.06]	Horizontal	5.2	5.3	37	38
169.8 [1.08]	Vertical	2.8	2.4	64	65
169.8 [1.08]	Horizontal	7.2	7.7	37	37

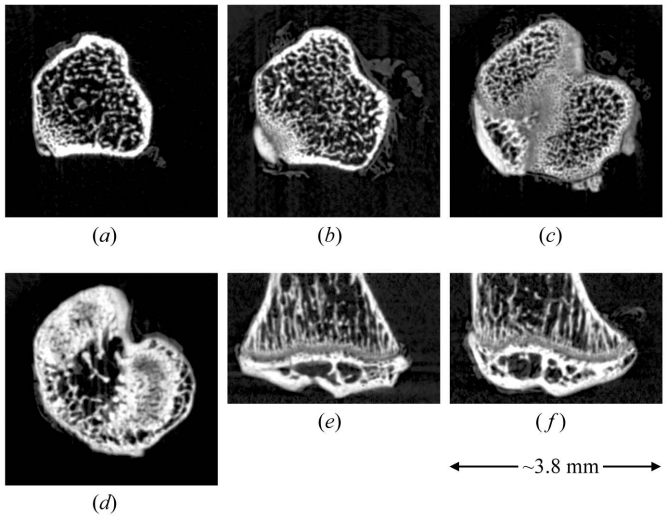

Figure 6
X-ray tomography reconstructed slices for a leptin-treated fixed mouse tibia. (*a*), (*b*), (*c*) and (*d*) show *xy* slices perpendicular to the main shaft of the bone at 1.72, 1.36, 0.99 and 0.62 mm, respectively, from the top of the tibia. (*e*) and (*f*) are *yz* and *xz* slices, respectively, at the longitudinal mid-line of the bone.

It can be shown that the contrast for a Gaussian-blurred edge can be expressed as

$$C = \frac{R'\lambda\left|\varphi t\right|}{2\pi(2\pi e)^{1/2}\sigma_{\rm tot}^2}, \tag{1}$$

and the resolution as

$$R = \left(4\sigma_{\rm tot}^2 + R'\lambda\right)^{1/2}, \tag{2}$$

where

$$\sigma_{\rm tot} = \left[\sigma_{\rm b}^2 + (M-1)^2\sigma_{\rm s}^2/M^2 + \sigma_{\rm d}^2/M^2\right]^{1/2}. \tag{3}$$

The derivation of these formulae and the associated validity conditions are detailed by Gureyev *et al.* (2008). $R' = R_1R_2/(R_1 + R_2) = R_2/M$ is the effective propagation or 'defocus' distance, λ is the X-ray wavelength, t is the thickness of the polyethylene, and $\sigma_{\rm b}$, $\sigma_{\rm s}$ and $\sigma_{\rm d}$ are the standard deviations associated with the blurring of the edge, the source emissivity

distribution ('source size') and the detector PSF, respectively. The second term on the right-hand side of (2) is associated with diffraction and is generally relatively small, but it may be significant in certain cases. These equations only relate to phase-contrast effects: neglecting absorption is justified in this case, *i.e.* the polyethylene sheet only absorbs 0.4% at 20 keV.

A non-linear least-squares refinement program [see Gureyev *et al.* (2008) for further details] was used to fit the experimental data given in Table 2 with the above equations. The parameters which can be refined are σ_b, σ_s(horiz), σ_s(vert), σ_d, t and the effective X-ray energy E. Given the limited amount of experimental data and the existence of significant correlations between certain parameters (t and E for example), the refined parameters were σ_s(horiz), σ_d and E. The value of φ was changed dynamically during the least-squares refinement as E was adjusted and was calculated using a density of 0.923 g cm^{-3}. The value of σ_b was fixed at 4 µm in accord with the findings of Gureyev *et al.* (2008) for the same plastic edges. Some preliminary refinements showed that σ_s(vert) was, as expected, quite small and so its contribution in (3), compared with the term involving σ_d, was insignificant. σ_s(vert) was therefore fixed at zero in subsequent refinements. The value of t was set to 100 µm. The refined values for the remaining parameters, giving equal weight to all 16 experimental data points, were as follows: σ_s(horiz) = 361 (9) µm, σ_d = 18.9 (0.3) µm and E = 18.4 (1.0) keV. The final fit to the experimental data was reasonable, as represented by an R-factor (Hamilton, 1965) value of 3.30% (see also the calculated values for contrast and resolution in Table 2), and the maximum correlation coefficient between refined parameters was only 0.40 [between σ_s(horiz) and σ_d]. The results obtained are very robust as large changes in the starting values for refined parameters produced no change in the final values. Fig. 7 shows the experimental intensity-profile data points corresponding to the M = 1.08 data summarized in Table 2. The solid curves are calculated using the Kirchhoff formula for the X-ray wavefunction including the parameter values detailed above. These theoretical curves include the effect of absorption in the polyethylene sheet and this effect can be seen in the experimental data points.

A least-squares refinement was also performed using a weighting scheme based on the e.s.d.s mentioned above, a given weight being the reciprocal of the square of the associated e.s.d. This has the realistic effect of giving significantly greater weight to the contrast values relative to the resolution values. The corresponding refined parameter values were σ_s(horiz) = 346 (14) µm, σ_d = 19.2 (0.5) µm and E = 18.0 (0.5) keV. Whilst these values have not changed markedly, the (weighted) R-factor is now 5.53%, indicating a poorer fit to the data (the standard goodness-of-fit parameter has a value of 1.13, the optimum value being unity). The maximum correlation coefficient is now 0.78 (between σ_d and E).

The refined value(s) of σ_s(horiz) is in good agreement with the nominal source size for the Australian Synchrotron (320 µm). If there was a significant degree of coherence across the spatial extent of the source we would expect the refined value(s) to be somewhat smaller than the design value. The value obtained for σ_d, which is equivalent to 44.6 (0.6) µm (unit weights case) in terms of FWHM, is somewhat larger than expected considering the specifications of the Gadox phosphor, but not unreasonable. It could be that some factor not accounted for in our model is causing an apparent degradation of the detector resolution, *e.g.* the presence of the Al filters and the associated scattered radiation (see, for example, Illers *et al.*, 2005). Lastly, the value of E that we obtain is reasonable considering the results shown in Table 1 and Fig. 2.

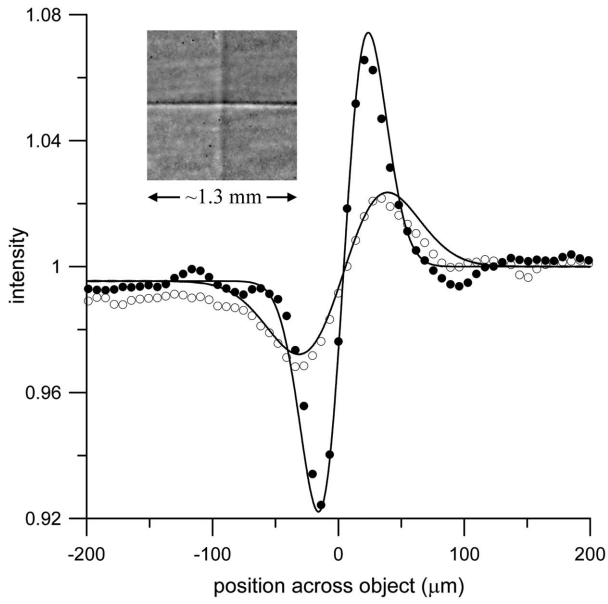

Figure 7
Experimental and calculated (Kirchhoff formula) intensity profiles for the M = 1.08 data summarized in Table 2. The solid data points and associated theoretical curve correspond to the profile across the horizontal plastic edge; the open data points and associated curve correspond to the vertical plastic edge.

4. Discussion and conclusions

The images and tomography results presented here show that the IMBL can produce high-quality data in a very simple 'barebone' experimental configuration. Given the plans for the implementation of a large number of imaging modalities in the coming years, we expect this facility to evolve to the forefront of X-ray imaging and tomography research, enabling world-leading contributions in fields ranging from biomedical and pre-clinical imaging to materials science [see, for example, Lewis (2005) and Stevenson *et al.* (2003), respectively]. The foremost science drivers are the acquisition of a superconducting multipole wiggler, the installation of custom-designed monochromators for high-resolution imaging and the development of beam focusing devices, in parallel with the commissioning of the long beamline to 136 m.

The preliminary results and analysis for the plastic-edge phantom give parameter values such as the horizontal source size in good agreement with expectations. An important finding is that, for the experimental configuration used, the

effective source size (horizontally) deduced from the images is close to the electron-beam size. The simple method used can be extended to encompass various X-ray optics, filters, detectors and other beamline components. Tests can readily be performed for different insertion-device gaps and filter combinations to characterize the source and the beamline.

Whilst the X-ray source size in the horizontal direction is large and the aspect ratio is 20:1, one needs to consider carefully the influence of other experimental parameters to quantify the imaging performance. For example, if $\sigma_b = 4$ μm, σ_s(horiz) = 400 μm, σ_s(vert) = 20 μm, $\sigma_d = 20$ μm and $M = 1.1$, equation (3) will yield σ_{tot}(horiz) = 41 μm and σ_{tot}(vert) = 19 μm, a ratio of only 2.2:1. However, a high-resolution detector with $\sigma_d = 2$ μm will yield values of 36 μm and 4.8 μm, respectively, a ratio of 7.7:1. In the first case, the detector resolution is the dominant factor vertically and the source size dominates horizontally. In the second case, the detector resolution and source size contributions are almost equal vertically and the source size is even more dominant horizontally. If we use $\sigma_d = 20$ μm, but with $M = 1.01$, σ_{tot}(horiz):σ_{tot}(vert) = 20.6:20.2 = 1.02:1. However, to achieve $M = 1.01$ with $R_1 = 20$ m requires $R_2 = 20$ cm and consequently significantly reduced phase contrast. This can be seen from the above equations as $R' \simeq R_2$ here and so the numerator in (1) will be significantly reduced. However, if $R_1 = 140$ m (IMBL satellite building), then $M = 1.01$ can be achieved with $R_2 = 1.4$ m and phase-contrast effects will be enhanced. It should be noted that this increase in R_2 (R') will also increase the diffraction term in (2). Finally, we should also point out that in these discussions the value of σ_b has been assumed to be quite small, as is the case for the polyethylene edges. In the case of 'real' objects, σ_b is likely to be significantly larger and it will have an important role to play, *e.g.* it may reduce detector-resolution requirements.

The present investigations identify useful operating conditions for the prevailing instrument parameters and constraints. Significant phase-contrast effects are observed and used quantitatively to determine and confirm values of these instrument parameters. Access to the satellite building for experiments in the near future will allow imaging with combined high spatial resolution and enhanced phase contrast, as well as a much larger field of view.

The authors thank Professor Jill Cornish of University of Auckland, New Zealand, for her support; the mouse tibiae samples were provided through a collaboration between one of us (DEM) and Professor Cornish. The authors are grateful to XRT Ltd for their encouragement of this work. We value discussions with Tim Gureyev and Yakov Nesterets of CSIRO, and Greg LeBlanc and Eugene Tan of the Australian Synchrotron. Many other Australian Synchrotron staff members helped us make these first experiments possible. Special thanks go to Alex Oggenfuss (on leave from the Swiss Light Source), Julian Price, Robert Grubb, Mark Clift, Bryce Karnaghan, Craig Millen, David Wang and Jason Wirthensohn.

References

Boldeman, J. W. & Einfeld, D. (2004). *Nucl. Instrum. Methods Phys. Res. A*, **521**, 306–317.
Clarke, J. A. (2004). *The Science and Technology of Undulators and Wigglers, Oxford Series on Synchrotron Radiation*, No. 4. Oxford University Press.
Cornish, J., Callon, K. E., Bava, U., Lin, C., Naot, D., Hill, B. L., Broom, N., Myers, D. E., Nicholson, G. C. & Reid, I. R. (2002). *J. Endocrinol.* **175**, 405–415.
Feldkamp, L. A., Davis, L. C. & Kress, J. W. (1984). *J. Opt. Soc. Am. A*, **1**, 612–619.
Gureyev, T. E., Nesterets, Ya. I., Stevenson, A. W., Miller, P. R., Pogany, A. & Wilkins, S. W. (2008). *Opt. Express*, **16**, 3223–3241.
Hamilton, W. C. (1965). *Acta Cryst.* **18**, 502–510.
Illers, H., Buhr, E., Günther-Kohfahl, S. & Neitzel, U. (2005). *Radiat. Prot. Dosim.* **114**, 214–219.
Lai, B., Khounsary, A. & Gluskin, E. (1993). Technical Bulletin ANL/APS/TB-11. Argonne National Laboratory/Advanced Photon Source, Argonne, IL, USA.
Lewis, R. A. (2005). *Nucl. Instrum. Methods Phys. Res. A*, **548**, 23–29.
Mills, D. M., Helliwell, J. R., Kvick, Å., Ohta, T., Robinson, I. A. & Authier, A. (2005). *J. Synchrotron Rad.* **12**, 385.
Paganin, D., Mayo, S. C., Gureyev, T. E., Miller, P. R. & Wilkins, S. W. (2002). *J. Microsc.* **206**, 33–40.
Snigirev, A., Snigireva, I., Kohn, V., Kuznetsov, S. & Schelokov, I. (1995). *Rev. Sci. Instrum.* **66**, 5486–5492.
Stevenson, A. W. *et al.* (2003). *Nucl. Instrum. Methods Phys. Res. B*, **199**, 427–435.
Tanaka, T. & Kitamura, H. (2001). *J. Synchrotron Rad.* **8**, 1221–1228.
Teague, M. R. (1983). *J. Opt. Soc. Am.* **73**, 1434–1441.
Wilkins, S. W., Gureyev, T. E., Gao, D., Pogany, A. & Stevenson, A. W. (1996). *Nature (London)*, **384**, 335–338.
Zschornack, G. (2007). *Handbook of X-ray Data.* Springer: Berlin.